



# Optimization of GMAW process parameters for weld overlay of Inconel 686 superalloy on low-carbon steel

Seyedmohammad Tabaie<sup>1</sup> · Trevor Greene<sup>2</sup> · Michael J. Benoit<sup>1</sup>

Received: 20 March 2023 / Accepted: 14 June 2023 / Published online: 1 July 2023  
© The Author(s), under exclusive licence to Springer-Verlag London Ltd., part of Springer Nature 2023

## Abstract

Weld overlays of Ni-based superalloys provide high-temperature corrosion, oxidation, and wear resistance for industrial applications. The objective of this study was to evaluate the microstructure of Ni–Cr–Mo superalloy Inconel 686 overlays fabricated using automatic gas metal arc welding (GMAW) with three different levels of voltage, travel speed, and wire feed speed. The variation of these parameters and their effects on the weld quality, dilution, and microsegregation were analyzed. The weld surface quality was assessed by visual examination. The weld dilution was measured by both geometric and chemical composition definitions. The maximum dilution was measured at 13.63%, induced by the highest weld heat input ( $5.97 \text{ kJ cm}^{-1}$ ) and lowest wire feed speed ( $6 \text{ m min}^{-1}$ ). The overlay dilution and the heat-affected zone (HAZ) size decreased by increasing the wire feed speed. However, increasing the wire feed speed and the heat input reduced the weld quality and even resulted in noncomplete joints. Microsegregation of elements was evaluated using energy-dispersive X-ray spectroscopy (EDS) analysis and it was found that microsegregation of Mo and Cr and the volume fraction of secondary phases in the interdendritic areas increased with increasing the weld heat input. According to the visual examination results and macro- and microscopic evaluation, the weld overlay parameters were found to be optimized for the mid-level heat inputs ( $4\text{--}5 \text{ kJ cm}^{-1}$ ) and wire feed speeds between 6 and  $8 \text{ m min}^{-1}$ .

**Keywords** Welding · Cladding · Inconel 686 · Dilution · Microstructure · Microsegregation · Process optimization

## 1 Introduction

Weld cladding, also known as weld overlay or hardfacing depending on application purposes, is a surfacing process in which a welding torch is used to deposit a layer (or multiple layers) of a material intended to enhance the wear or corrosion resistance of a generally lower cost and lower performance structural alloy (e.g., steel) [1, 2]. The weld overlay process can also be applied to ‘build up’ and repair worn components to increase service life [3]. This technique has been applied for various applications in the mining and mineral processing sectors [2]. Due to the fact that in many cases only the internal surface of a component is exposed to a corrosive environment, and so only that surface needs

to be protected, savings on material costs can be achieved by taking advantage of the weld overlay technique [2]. Conventional arc welding technologies, such as shielded metal arc welding (SMAW), gas metal arc welding (GMAW or MIG/MAG), and gas tungsten arc welding (GTAW or TIG) are widely employed as heat sources to deposit high-performance filler metals on different base metal (BM) substrates [2], due to the fact that these technologies are relatively inexpensive, flexible, easy to implement for field applications, broadly available, etc.

Beginning in the 1960s, highly corrosion-resistant nickel–chromium–molybdenum (Ni–Cr–Mo) alloys (e.g., Inconel 625 [4], Inconel 686 [5], alloy C-22 [6], and Hastelloy C-276 [6]) have been developed to operate in the most severe corrosive environments [3, 7]. Superalloy Inconel 686 (IN686) was developed in 1992 and was derived from conventionally employed alloy C-22 and C-276 due to the relatively low oxidation resistance of these alloys. Inconel 686 is an austenitic single-phase, solid solution strengthened nickel–chromium–molybdenum–tungsten (Ni–Cr–Mo–W) based superalloy [5]. Inconel 686 alloy is extensively used in

✉ Seyedmohammad Tabaie  
smotabaie@gmail.com

<sup>1</sup> School of Engineering, University of British Columbia, Kelowna, BC V1V 1V7, Canada

<sup>2</sup> Teck Resources Limited, Trail, BC V1R 4L8, Canada

the chemical processing, marine, petrochemical, mining, and oil and gas industries, for applications such as internal cladding of pipes, boilers, pressure vessels, and chemical reactors [5, 8, 9]. The presence of chromium (Cr) and molybdenum (Mo) in IN686 provides good resistance to oxidizing and reducing environmental damages; Cr is responsible for forming a surface oxide layer, while Mo increases resistance to localized corrosion by promoting re-passivation of the oxide film [10, 11]. The carbon (C) content of IN686 is restricted to 0.01 wt.%, which facilitates retardation of grain boundary precipitation in the heat-affected zone (HAZ) of welded areas to uphold the corrosion resistance [5]. Consequently, IN686 is endowed with exceptional resistance to oxidizing, reducing, and mixed acid environments including those containing halides. IN686 alloy is also used in order to avoid field post-weld heat treatment (PWHT) due to bead tempering effects of the HAZ, which does not show a classical coarse grain microstructure and avoiding unnecessary phase transformation (specifically in low heat input GMAW) [12]. However, due to non-equilibrium solidification rates in welding and certain alloying elements present in amounts that are beyond the solubility limit of the austenitic matrix (e.g., Mo, W, Cr), brittle secondary particles known as topologically close-packed (TCP) phases may be formed, which include the  $\sigma$ , P, and  $\mu$  phases [3, 4, 8].

Silva et al. [8] used automatic GTAW along with a separate wire feeding unit to supply AWS ER-NiCrMo-14 wire (similar to IN686 alloy) to create a multi-bead weld overlay on an ASTM A516-Gr 60 substrate. They reported microsegregation of Cr, Mo, and W during solidification and detrimental effects of TCP phases on the corrosion properties of the overlay. Mina et al. [10] used the same method and materials as Silva et al., and calculated the variation of dilution (compositionally and geometrically) by changing the welding pattern and wire feed speed (WFS) at a constant heat input (HI) (i.e., constant current (I), voltage (V), and weld or travel speed (TS)). They reported that the dilution of the overlays increased from 14.3 to 33.3% by reducing the WFS from 8.5 to 4.5 m min<sup>-1</sup>, as less filler metal was deposited per unit length of weld but with fairly consistent base metal melting due to the constant heat input (15.27 kJ cm<sup>-1</sup>). Iron (Fe) showed greater potential to be incorporated into the primary solid phase during solidification, and the Fe level was found to increase with the increase of dilution. Conversely, Cr, Mo, and W showed a slight decrease in their partition coefficients (k) with the increase of the dilution. A high amount of dilution (on the average more than 20%) was reported in both studies by using the GTAW technique.

Conversely, the GMAW technique results in greater filler metal deposition, due to a continuous wire feeding process, and is attracting more attention for weld overlays in industrial applications [13–16]. GMAW reduces the amount of the dilution (by increasing arc efficiency and inducing

lower heat input [13]) and increases the surface quality of the overlay, which consequently enhances the weld overlay corrosion resistance. Najafi et al. [16] reported a maximum of 13% dilution in the fusion zone by using the GMAW for IN625 overlay, as measured by Fe content in the weld overlay, which was less than the minimum dilution observed for GTAW overlays as noted above. Petrzak et al. [17] used a hybrid technique, cold metal transfer (CMT) and GMAW, for the weld overlays of IN686 and IN625. They considered two different WFSs of 0.7 and 0.8 m min<sup>-1</sup>, which are very low feeding rates in industrial-scale weld overlay but resulted in weldments with no imperfections and only 2% and 1% Fe content in the fusion zone of welded IN625 and IN686, respectively. However, variation of GMAW process parameters and their effects on microsegregation and formation of TCP phases have not been discussed in literature.

According to the literature, there is a lack of scientific information about the relationships between automatic GMAW parameters (specifically wire feed speed) and the resultant microstructure and weld quality for weld overlays of IN686. The objective of the present study is to investigate on the effects of variation of GMAW parameters on the resultant weld overlay quality, with a particular focus on the weld metal (WM) and BM microstructure. The microstructural evolutions, such as compositional dilution, solidification microstructure of the WM, microsegregation of elements, and phase transformation in the BM, are correlated with the evolution of microhardness, and the obtained results are used to develop a process map to optimize GMAW parameters for the weld overlay of IN686.

## 2 Experimental procedures

### 2.1 Materials

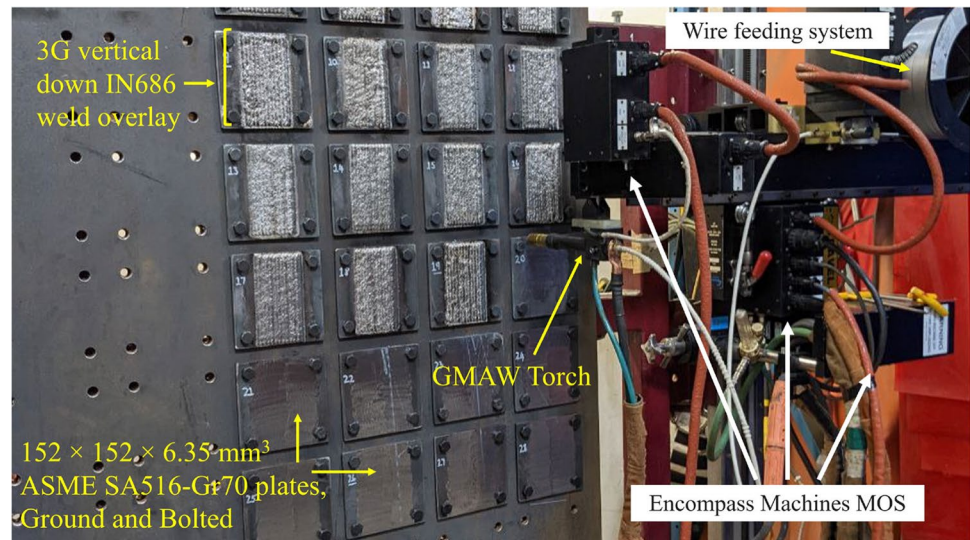
An AWS ER-NiCrMo-14 wire (equivalent to IN686) with a diameter of 1.143 mm was supplied by Special Metals Co. and was applied as the filler metal. The weld overlay substrates were low-carbon steel ASME SA516-Gr.70 plate with dimensions of 152.4 × 152.4 × ~6.35 mm<sup>3</sup> and the surface of the plates were ground prior to welding. Table 1 shows the chemical composition of the as-received materials.

### 2.2 Welding process and design of experiment

The weld overlays were fabricated using an Encompass Machines, Inc. semi-automated MIG overlay system (MOS), which is used to control torch movement, and the system was equipped with a Miller Electric 350 MPA weld power supply and automatic wire feeding system, as shown in Fig. 1. For the purposes of this study, weld overlays were fabricated using a 3<sup>3</sup> design of experiment

**Table 1** Chemical composition of the filler metal and base metal (wt.%)

Materials	Ni	Fe	Mo	Cr	W	Mn	Al	Ti	C	Si	Cu	S	P
ER-NiCrMo-14 (Filler wire)	Bal	0.28	16.4	20.5	3.6	0.27	0.27	0.09	0.007	0.05	0.01	<0.001	0.001
SA516—Gr.70 (Substrate)	0.16	Bal	–	0.17	–	1.184	–	0.002	0.157	0.343	0.131	0.002	0.012

**Fig. 1** Controlled and automatic GMAW overlay process on fixed plates in the vertical down (3G) position

based on Taguchi's L27 orthogonal array in which the arc voltage ( $V$ ), torch travel speed ( $TS$ ), and wire feed speed ( $WFS$ ) were all varied between three levels for a total of 27 overlay conditions as shown in Table 2. The MOS and power supply were not synergic, allowing for independent control of the current ( $I$ ) and wire feed speed. Thus, the weld current was adjusted prior to the deposition of each weld overlay to achieve weld beads with a reasonable profile as judged by the system operator. Therefore, the total heat input per unit length (HI) is specified in Table 2 for all conditions, where:

$$HI = \frac{60 \times I \times V \times \eta}{1000 \times TS} \left( \frac{\text{kJ}}{\text{cm}} \right) \quad (1)$$

In which  $\eta$  is process arc efficiency ( $\sim 0.85$  for GMAW). The welding current,  $TS$ , and  $V$  were maintained in real-time by a data acquisition system to ensure the required heat input during cladding production. The MOS system tried to control and maintain the current individually at an average value of 190 A for all welding conditions. The HI is reported as linearly related to the  $WFS$ , which affects dilution and weld bead geometry [18]. Nevertheless, the effects of the  $WFS$  on welding heat input and dilution are studied in this research. Argon shielding gas at a flow rate between 17 and 18 L/min was used for fabrication of the overlays. The weld overlays were fabricated in the vertical down (3G) position, in which the plates were fixed

to a vertical wall by bolts at the four corners of the plate as shown in Fig. 1. A triangular weave with a horizontal arc amplitude of 3 mm was used during welding to mitigate defects [10]. Each weld overlay was comprised of 12 overlapping tracks, where the overlap distance was equal to half of the measured bead width for the specific parameter set as shown schematically in Fig. 2. No base plate pre-heat was employed during the overlay procedure, but an interpass temperature between 200 to 300 °C was used between deposition of adjacent tracks. Two experiments (#22 and #25 in Table 2) were not welded, due to the high HI and low  $WFS$  ( $6 \text{ m min}^{-1}$ ), which resulted in melting the wire to the tip of the torch.

### 2.3 Dilution and microstructural analysis

Samples from the weld overlay plates were cut by water jet (Fig. 3 a and b) and subjected to conventional metallographic preparation, specifically to be able to acquire a cross-section macrograph, as well as for microstructure analyses by optical digital microscopy (Keyence VHX-970F) and scanning electron microscopy (SEM) using a Tescan Mira 3 XMU equipped with an energy dispersive spectroscopy (EDS) detector. Chemical etching was performed with Marble reagent to reveal the BM section while electrolytic etching was performed with a 10% solution of chromic acid at 2 V for 15–20 s to evaluate the microstructure of the WM section (IN686 alloy).

**Table 2** Taguchi L27 DoE factors and levels and the corresponding calculated HI

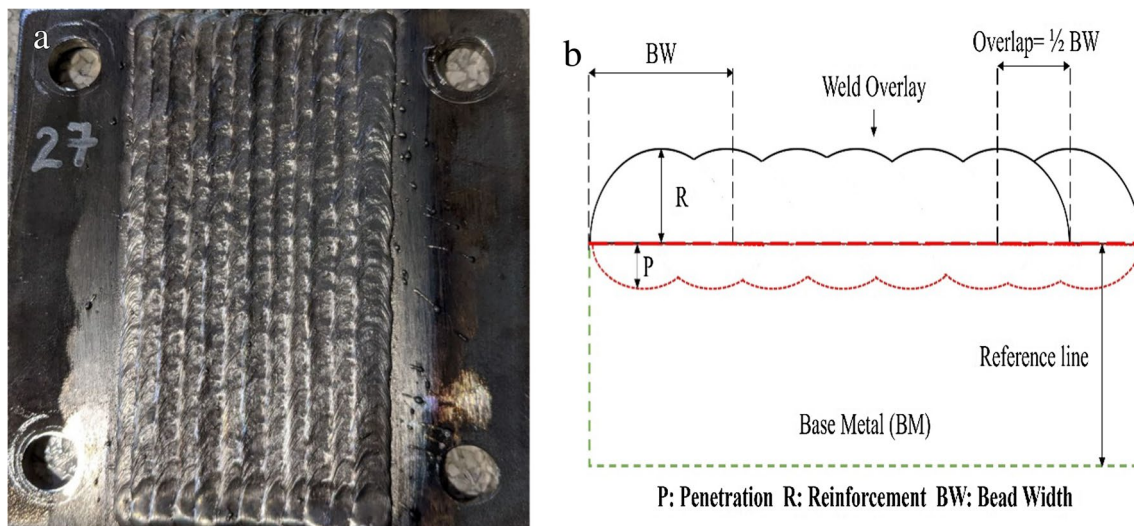
Sample #	V (V)	TS (cm/min)	WFS (m/min)	HI (kJ/cm)
1	19	40.6	6	4.53
2	19	40.6	8	4.53
3	19	40.6	10	4.53
4	19	45.7	6	4.03
5	19	45.7	8	4.03
6	19	45.7	10	4.03
7	19	50.8	6	3.62
8	19	50.8	8	3.62
9	19	50.8	10	3.62
10	22	40.6	6	5.25
11	22	40.6	8	5.25
12	22	40.6	10	5.25
13	22	45.7	6	4.66
14	22	45.7	8	4.66
15	22	45.7	10	4.66
16	22	50.8	6	4.2
17	22	50.8	8	4.2
18	22	50.8	10	4.2
19	25	40.6	6	5.97
20	25	40.6	8	5.97
21	25	40.6	10	5.97
22	25	45.7	6	5.30
23	25	45.7	8	5.30
24	25	45.7	10	5.30
25	25	50.8	6	4.77
26	25	50.8	8	4.77
27	25	50.8	10	4.77

The weld geometries were measured by using ImageJ software on macrographs obtained from the cross-sectioned samples. The dilution of the weld overlay plates was calculated and obtained by two methodologies. In the first method, the geometrical characteristics of the claddings were used, namely the areas of the fusion zone in base metal (B in Fig. 3 c) and the weld metal, above the weld interface (A in Fig. 3 c), which composed the melted region. The reference line (RL) was considered as the top of the nominal plate thickness (Fig. 3 b, c). Equation (2) shows the formula used to calculate the geometric dilution (Geo. D), while conservation of mass was used to calculate the compositional dilution (Com. D) in Eq. 3. The concentrations of Fe in the welded zone ( $Fe_{wz}$ ), in the BM ( $Fe_{BM}$ ), and in the filler metal ( $Fe_{fm}$ ) were obtained by EDS measurement and calculation of Com. D was performed for the samples with the maximum, average, and minimum Geo. D.

$$\text{Geo. D}(\%) = \frac{B}{A + B} \quad (2)$$

$$\text{Com. D}(\%) = \frac{Fe_{wz} - Fe_{fm}}{Fe_{BM} - Fe_{fm}} \quad (3)$$

Optical microscopy, SEM analysis, and EDS measurements were made over large areas of the FZ (the area that the filler metal melted and diffused to the BM) and the WM, in order to evaluate solidification microstructure (i.e., dendrite arm spacing or DAS) and to obtain the global FZ chemical composition of each overlay. Volume fraction of particles was measured by ImageJ software. All the parameters used followed the recommendations of the ASTM E1245 standard [19]. Furthermore, all the results were analyzed according to

**Fig. 2** a An example of a weld overlay sample (sample #27) and b a schematic of the weld geometry measurement

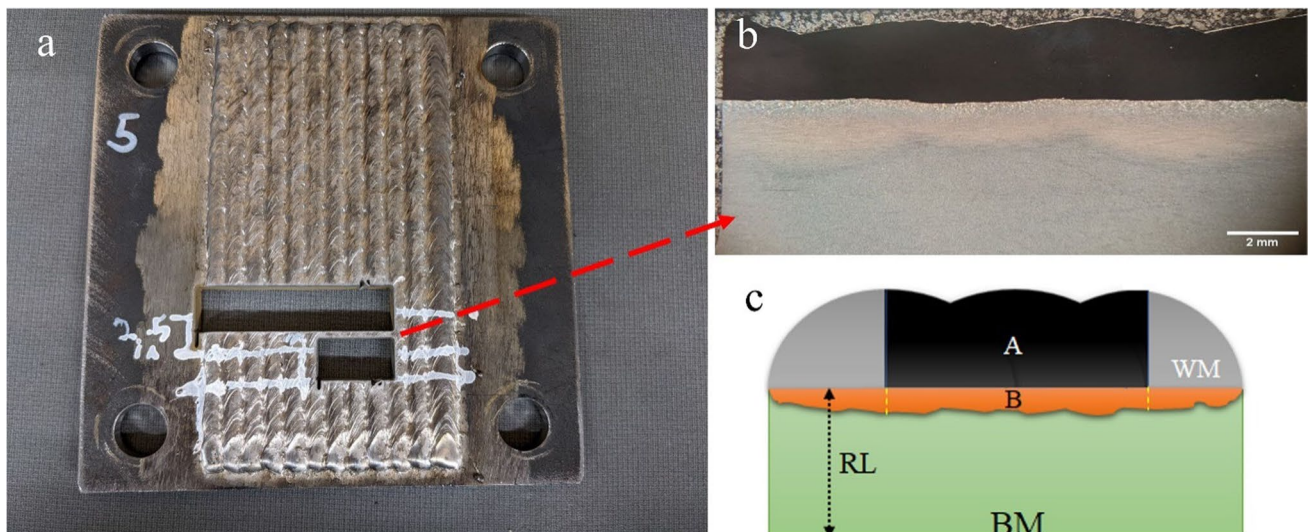


**Fig. 3** **a** A weld overlay sample with transverse cut by water-jet, **b** optical macroscopy of the transverse cut sample, and **c** the selected areas for geometric dilution calculation

the ASTM E1245 standard at the 95% confidence level for all results to be comparable with the literature [10].

#### 2.4 Microhardness measurement

After revealing the microstructure of all zones (e.g., WM, FZ, HAZs, and BM), Vickers microhardness method was used to analyze the hardness evolution from the top of the WM to the bottom part of the BM of all samples. A Wilson VH3100 automated Vickers hardness machine with a load of 1 kg and a dwell time of 10 s was used for the measurements. A total of 3 to 5 indentations were performed in each zone for all conditions to evaluate the variability in the measured hardness value.

### 3 Results

#### 3.1 Visual examination

Examples of typical weld overlay plates are shown in Figs. 3 and 4 a and b. Some defects such as discrete weld lines (i.e., lack of fusion with the adjacent weld bead), porosity on the weld surface, spattering, and generally low surface quality were found on some weldments as can be seen in Fig. 4 a and b. Table 3 presents the results of the qualitative visual examination for all samples. No cracks or undercut were observed by visual inspection for any welding conditions studied. In some samples, discontinuity in the weld bead and/or discrete weld lines (i.e., lack of fusion with adjacent

**Fig. 4** Examples of **a** discrete weld line defects (no overlap) and **b** spattering as observed by visual examination

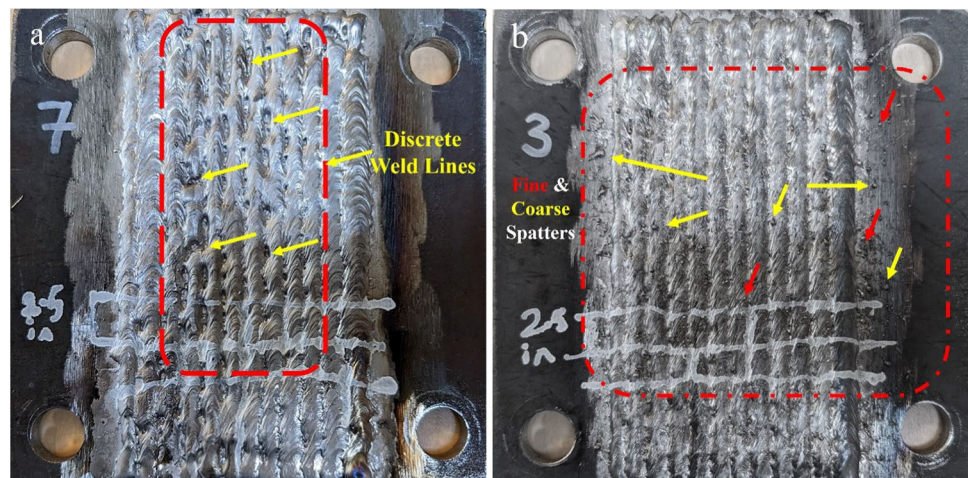


**Table 3** Visual examination results for all weld overlay conditions. Note that samples 22 and 25 are not included as a weld was not able to be successfully formed

S#	Voltage (V)	TS (cm/min)	WFS (m/min)	HI (kJ/cm)	Spatter	Surface Porosity	Discrete weld lines	Surface quality
1	19	40.6	6	4.53	1	–	–	Great
2	19	40.6	8	4.53	3	–	–	Fair
3	19	40.6	10	4.53	5	–	–	Bad
4	19	45.7	6	4.03	1	–	–	Great
5	19	45.7	8	4.03	3	–	–	Fair
6	19	45.7	10	4.03	4	Yes	Yes	Bad
7	19	50.8	6	3.62	1	Yes	Yes	Bad
8	19	50.8	8	3.62	3	Yes	–	Fair
9	19	50.8	10	3.62	4	–	Yes	Bad
10	22	40.6	6	5.25	3	Yes	Yes	Bad
11	22	40.6	8	5.25	3	–	–	Fair
12	22	40.6	10	5.25	5	–	–	Bad
13	22	45.7	6	4.66	1	–	–	Great
14	22	45.7	8	4.66	3	–	–	Fair
15	22	45.7	10	4.66	5	Yes	Yes	Bad
16	22	50.8	6	4.20	2	Yes	–	Great
17	22	50.8	8	4.20	2	–	–	Great
18	22	50.8	10	4.20	2	–	–	Great
19	25	40.6	6	5.97	2	Yes	–	Bad
20	25	40.6	8	5.97	2	Yes	–	Fair
21	25	40.6	10	5.97	3	Yes	–	Fair
23	25	45.7	8	5.30	3	–	–	Great
24	25	45.7	10	5.30	5	–	–	Fair
26	25	50.8	8	4.77	3	–	–	Great
27	25	50.8	10	4.77	3	–	–	Great

weld bead) caused by a suboptimal combination of welding conditions was observed (Fig. 4 a).

The spattering performance and level of each plate was qualitatively categorized into five levels (as provided in Table 3): Level 1 means no spattering, 2: few amounts of fine spatters, 3: few amounts of coarse spatters, 4: high numbers of fine spatters, and 5: high numbers of coarse spatters (i.e., a mixture of fine and coarse spatters) (Fig. 4 b). The effect of spattering on the overlay microstructure is further discussed in Section 4. The surface quality of overlay plates is also qualitatively categorized into 3 levels: great (i.e., no spatter, no discrete weld lines, no porosity, and a smooth surface), fair (i.e., smooth surface with few amounts of fine spatters), and bad (i.e., non-uniform surface, discrete weld lines, surface porosity, and many fine and coarse spatters) (Table 3).

### 3.2 Welding geometries and dilution

The geometries of the weld beads (i.e., bead width, penetration, and weld reinforcement) and area of the HAZ were measured from the transverse cross sections samples

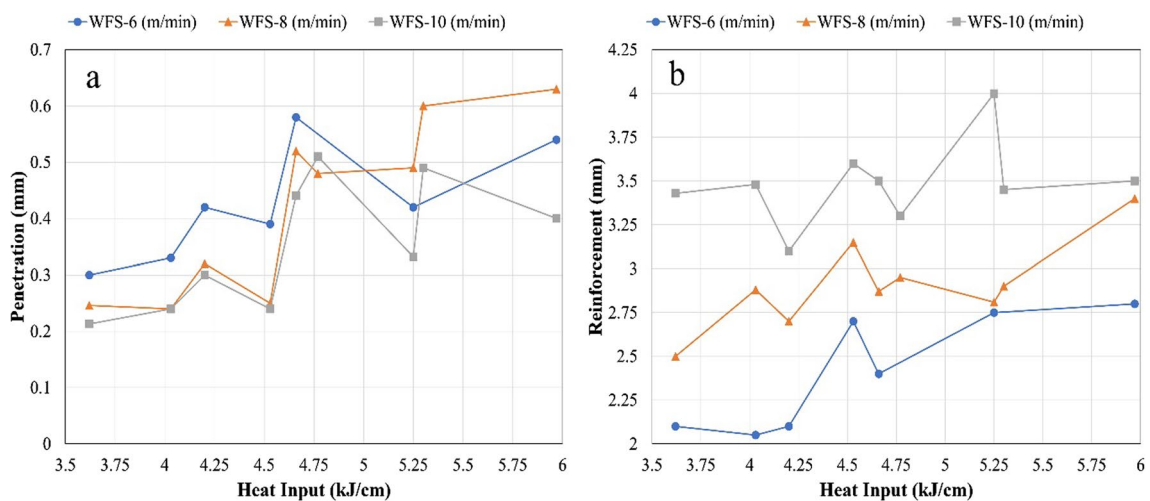
extracted from each welded plate using Keyence VHX-970F digital microscope and ImageJ software. Table 4 shows the weld bead geometries, the maximum thickness of the HAZ (all zones), and the calculated Geo. D and Com. D for each sample as a function of the HI. Note that Com. D was measured only for select conditions corresponding to the minimum, maximum, and average Geo. D.

Figure 5 a and b shows the variations of the bead reinforcement ( $R$ ) and the penetration ( $P$ ) by changing the WFS and the HI. The results demonstrate that when the HI increased, both  $P$  and  $R$  generally increased for each WFS value, but the WFS induced different trends. Increasing the WFS slightly reduced the  $P$  values (Fig. 5 a) while significantly increasing the  $R$  values (Fig. 5 b), which is reasonable as more mass is deposited per unit length and, thus, more heat input is used to melt the wire with increasing WFS rather than melting the substrate.

Figure 6 a–c depicts the variations of the Geo. D vs. the arc voltage for different WFSs and constant TS, to provide separate interpretation on the effect of the voltage on dilution. As can be seen from Fig. 6 a–c, the dilution increased with increasing voltage for all three wire feed

**Table 4** Weld overlay geometries and calculated geometric and compositional welding dilution

Sample #	HI (kJ/cm)	BW (mm)	P (mm)	R (mm)	HAZ (mm)	Geo. D (%)	Com. D (%)
1	4.53	12.0	0.39	2.71	2.20	9.61	12.43
2	4.53	12.3	0.25	3.15	1.90	8.10	–
3	4.53	13.2	0.24	3.60	1.80	5.19	4.99
4	4.03	11.8	0.33	2.05	2.00	8.99	–
5	4.03	12.4	0.24	2.88	1.70	6.64	–
6	4.03	13.0	0.24	3.48	1.70	5.29	–
7	3.62	11.65	0.30	2.11	1.77	7.80	9.14
8	3.62	12.5	0.25	2.50	1.82	6.01	–
9	3.62	13.0	0.21	3.43	1.60	5.15	6.44
10	5.25	12.5	0.42	2.75	2.55	10.95	8.88
11	5.25	12.2	0.49	2.81	2.47	10.00	–
12	5.25	12.6	0.33	4.00	1.75	6.06	–
13	4.66	12.4	0.58	2.40	2.40	9.51	–
14	4.66	12.5	0.52	2.87	1.93	8.24	3.77
15	4.66	13.5	0.44	3.50	1.80	6.61	–
16	4.20	12.3	0.42	2.10	1.96	8.45	–
17	4.20	13.3	0.32	2.70	1.72	7.03	–
18	4.20	13.6	0.30	3.10	1.80	6.48	–
19	5.97	12.7	0.54	2.80	1.30	4.22	7.89
20	5.97	12.7	0.63	3.40	2.90	13.63	11.21
21	5.97	12.8	0.40	3.50	3.00	7.09	–
23	5.30	12.3	0.60	2.90	2.23	9.34	8.77
24	5.30	13.0	0.49	3.45	1.80	7.13	–
26	4.77	13.1	0.48	2.95	2.30	8.34	–
27	4.77	12.8	0.51	3.31	2.10	7.43	–



**Fig. 5** Variation of **a** welding penetration and **b** reinforcement with the welding heat input and the various WFSs studied

speeds and at all travel speeds. Besides, the dilution generally decreased when the TS increased for a given WFS and  $V$  (Fig. 6 d–f). However, the dilution remained nearly constant as  $TS$  increased when the  $WFS$  was at maximum value ( $10 \text{ m min}^{-1}$ ).

Figure 7 shows the overall effect of the main welding parameters (i.e.,  $V$ ,  $TS$ , and  $I$ ), through the total heat input, on the dilution for different wire feeding rates. In general, the dilution increased with increasing HI, although this trend was more obvious for lower  $WFS$  values of 6 and 8  $\text{m min}^{-1}$ .

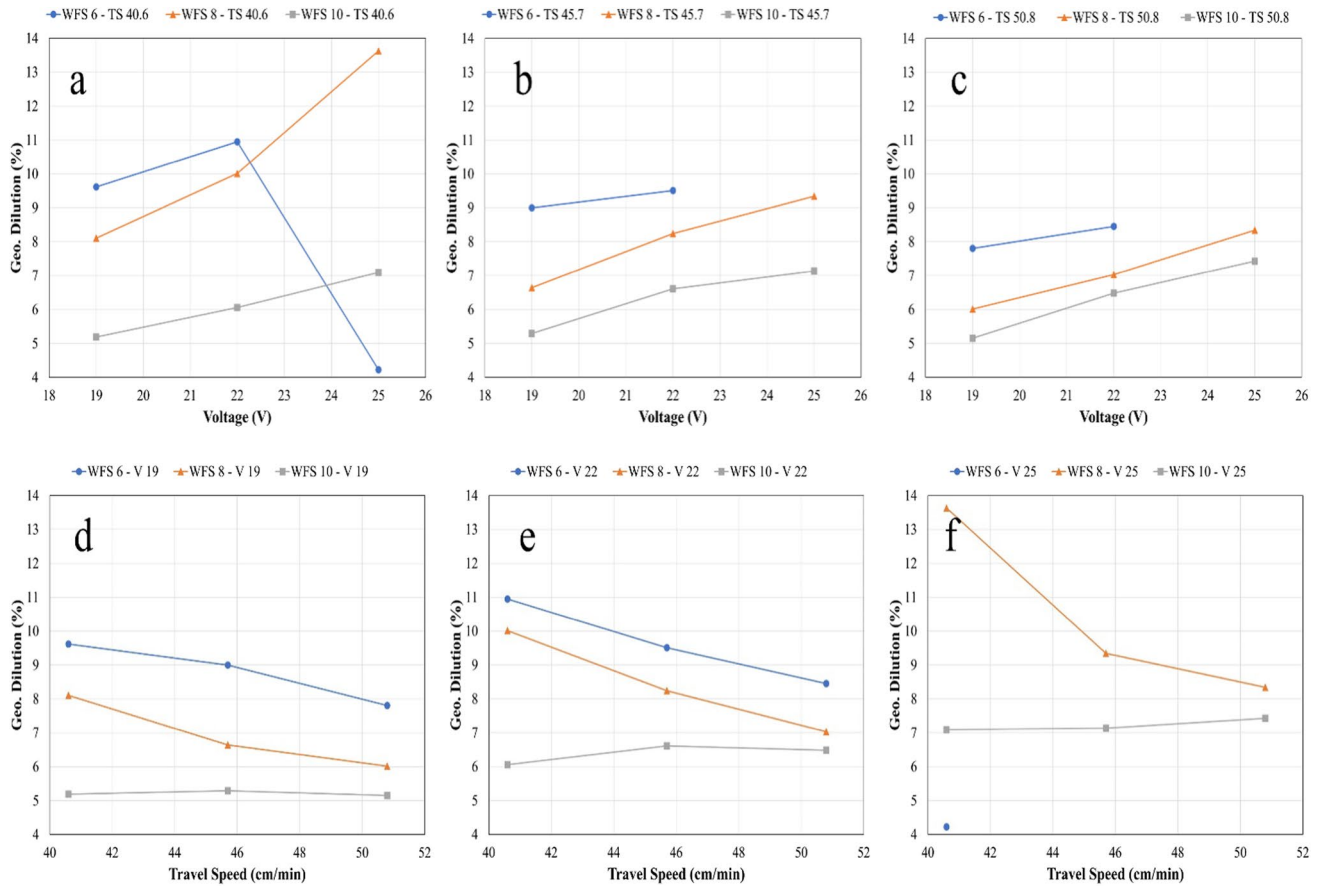


**Fig. 6** Geo. dilution **a–c** as function of voltage for the different wire feed speeds and at constant travel speeds and **d–f** as function of travel speed for the different wire feed speeds and at constant voltage

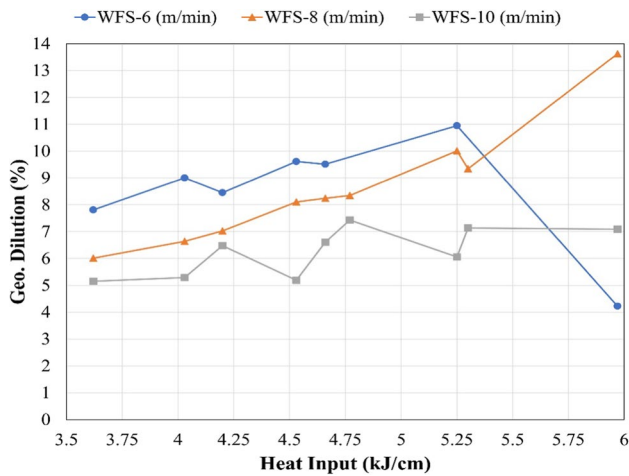


**Fig. 7** Geo. dilution plotted as a function of welding heat input for different wire feed speed levels

Conversely, the effect of *HI* on the geometric dilution was less pronounced at the highest *WFS* of 10 m min<sup>-1</sup>. For instance, the dilution decreased from 9.5% (S#13) to 6.6%

(S#15), at *HI* = 4.66 kJ cm<sup>-1</sup> by increasing the *WFS* from 6 to 10 m min<sup>-1</sup>, respectively.

The dilution of S#19 (*V*: 25 V, *TS*: 40.6 cm min<sup>-1</sup>, *WFS*: 6 m min<sup>-1</sup>, *HI* = 5.97 kJ cm<sup>-1</sup>) was found to be the minimum value (4.22%) among all conditions, despite corresponding to the highest *HI* and lowest *WFS* value studied. Since the welding with the low *WFS* (e.g., 6 m min<sup>-1</sup>) and the higher *TS* failed for samples #22 and #25 (Table 2), the microscopic evaluation of S#19 in the weld zone revealed that the joint was not complete at the weld interface and, consequently, the penetration and dilution were very small.

The geometrical dilution (Geo. D) and the dilution based on EDS Fe composition measurements (i.e., Comp. D) are reported in Table 4. Besides, Fig. 7 shows the alteration of Geo. D by increasing the *HI* for different wire feed speeds. The dilution increased in all samples by increasing the heat input, except for a sample with the highest *HI* (5.97 kJ cm<sup>-1</sup>) and the lowest *WFS* (6 m min<sup>-1</sup>) which is discussed before. Samples with the highest *WFS* (10 m min<sup>-1</sup>) produced the lowest Geo. Dilutions for all *HI* values. The Fe concentration in the fusion zone and the corresponding Comp. D for samples #3 and #9 with



the WFS  $10\text{ m min}^{-1}$  revealed very low dilution of 4.99% and 6.44%, respectively, which are close to their respective measured Geo. D (Table 4). Comparison between the Geo. D and Com. D reveals the presence of a little difference (e.g., S#10 and #14), which has been also reported by [8, 10] and can be attributed to the EDS point analysis for Com. D and relative area measurement for Geo. D.

Figure 8 shows an EDS map and line-scan analysis of the chemical composition profile obtained from the weld interface of sample #23 (Geo. D: 9.34%, Com. D: 8.77%). The

line scan and elemental mapping results from the EDS analysis show a steep transition of Fe from the steel BM to the weld metal in the vicinity of the weld interface. It is worth mentioning that there is a reverse step change/concentration gradient for Ni, Cr, and Mo at the interface. It is critical to understand the local change in composition induced in the weld metal due to base metal dilution, as alteration of the weld metal chemical composition can manipulate the phase transformation and formation of the TCP phases, which mainly contain Fe, Mo, and Cr [2, 8, 20].

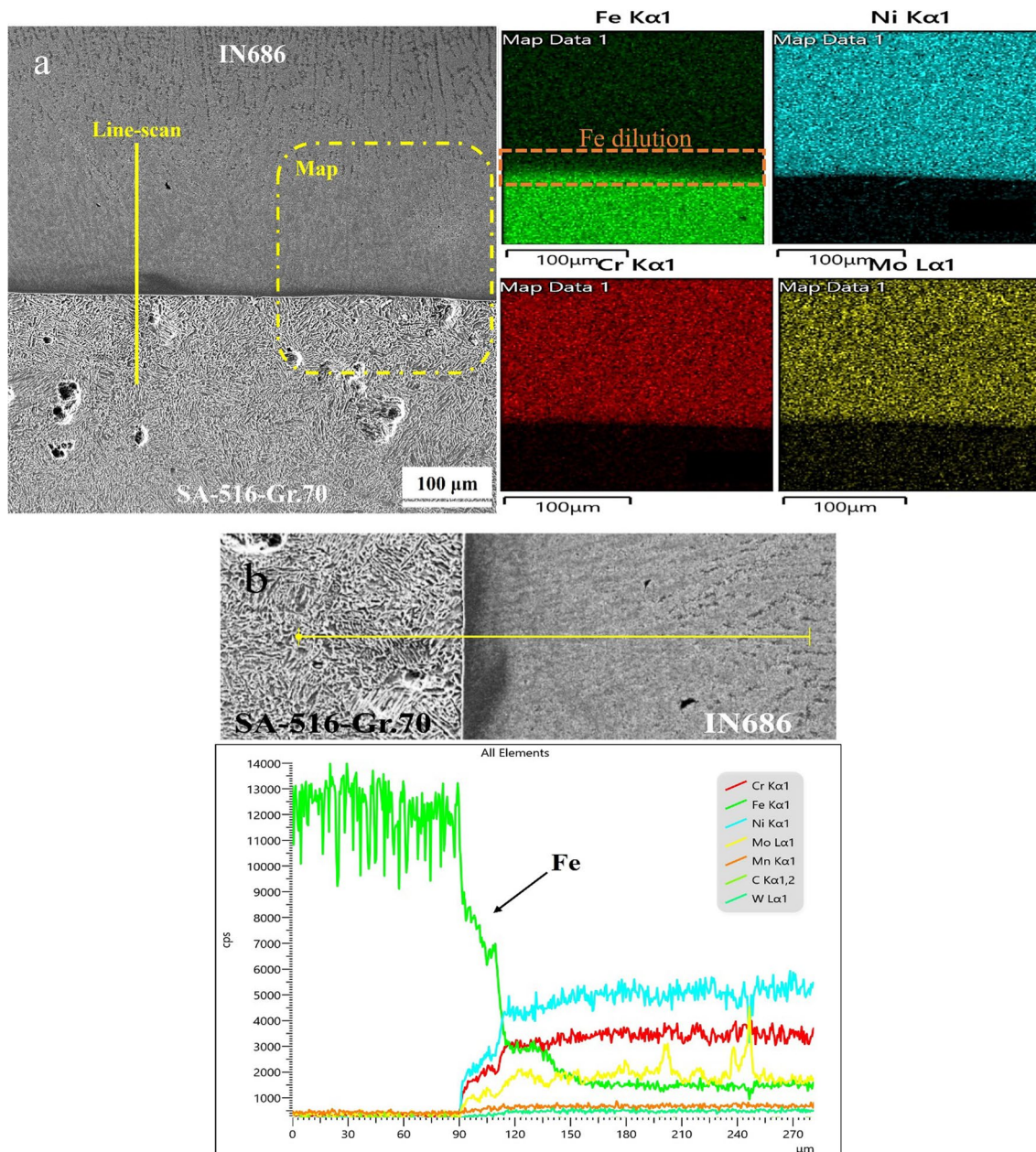


**Fig. 8** **a** EDS elemental map analysis of the Fe dilution in the weld metal and **b** EDS line-scan analysis of the variation of elements from the BM toward the WM, taken from S#23

### 3.3 Microstructural evolution

This section details the microstructural features observed during the microscopic analysis of the applied overlay alloy IN686 and the base material for different conditions in this study. Few studies on weld overlay via the GMAW technique of IN686 were found in the literature and, of these, almost none provided any details of the microstructure evolution, instead only reviewing their corrosion resistance properties. Thus, the current results present a greater emphasis on the microstructure of the weldments in order to provide a better understanding of the metallurgical aspects and, thus, contribute to the scientific and technological knowledge of the IN686 cladding on a substrate.

#### 3.3.1 The base metal

According to the heat input variation, the base metal microstructure can be categorized into different heat-affected areas. From the weld metal interface toward the BM, 5 different zones were identified (Fig. 9): Weld zone (WZ)-HAZ 1, HAZ 2, HAZ 3, the HAZ to BM transition region, and finally the BM.

The comparison of microstructures observed in the different HAZs is shown in Fig. 10 (S#10, HI:  $5.25 \text{ kJ cm}^{-1}$ ). The HAZ mainly consists of three different microstructural regions: coarse-grained HAZ (WZ-HAZ 1, HAZ 2), fine-grained HAZ (HAZ 3), and transitional zone. Figure 10 a shows the WZ-HAZ 1 region, which is directly adjacent to the weld interface (fusion zone), and is significantly affected by welding heat input, with peak temperatures ranging from 900 to 1400 °C, which is appropriate for both austenitization and grain growth [21]. The major phase components in HAZ1 include dominantly acicular ferrite (AF), primary ferrite (PF), Widmanstätten ferrite (WF), upper bainite (UB), pearlite, and lath martensite (M) (due to the rapid heating and cooling), all of which have been previously observed

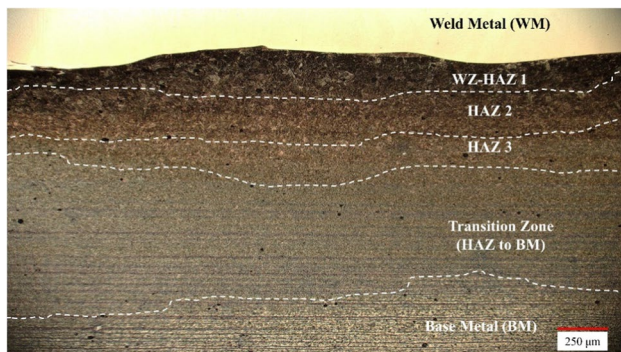


**Fig. 9** An optical micrograph of as-welded S#10 from the weld metal and weld zone (WZ) to the base metal (BM), delineating the different HAZs

in welding of this steel substrate [22]. Below this region is HAZ2, which reaches a peak temperature between  $AC_3$  (790 °C) and 1100 °C. As can be seen in Fig. 10 b, the HAZ 2 contained AF, WF, pearlite, and ferrite with finer grains than the HAZ 1 due to the lower heat input. The HAZ3 occurs when the heat input results in a BM peak temperature between  $AC_1$  (670 °C) and  $AC_3$  (790 °C), resulting in austenitization. However, substantial grain growth does not occur in the HAZ 3 due to a faster cooling rate, which leads to a fully recrystallized (RX) and a fine-grained microstructure (ferrite + pearlite), as seen in Fig. 10 c. The observations also revealed that there was a transitional zone between the HAZ 3 and the BM in which partial recrystallization occurred at the grain boundaries of primary grains (i.e., ‘necklaces’ of RX grains [23]) (Fig. 10 d). Figure 10 e and f shows the OM and SEM micrographs of the unaffected BM, respectively, which contains ferrite and pearlite as well as the microstructure features of the as-received plates (i.e., rolling bands). Therefore, the final appearance of HAZ depends upon the heat input, peak temperature, and cooling rate (depending on the welding heat input).

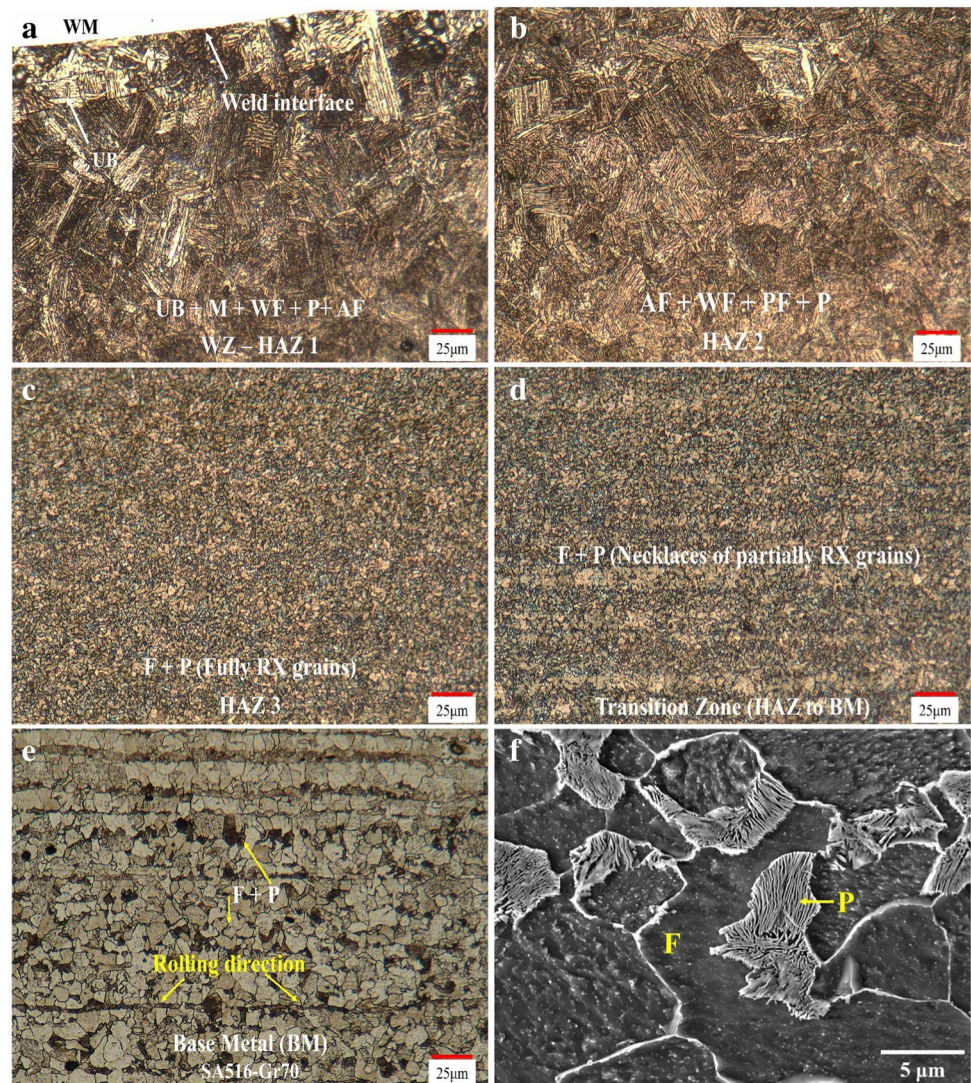
In all samples, the microstructure depends primarily on the chemical composition and cooling rate or the HI. The HI during welding affects the phase transformation and extent of grain refinement from the primary grains during recrystallization in the BM and the HAZ zones. Figure 11 shows a comparison of the grain refinement in the lowest HI (i.e.,  $3.62 \text{ kJ cm}^{-1}$ , S#8) and the highest HI (i.e.,  $5.97 \text{ kJ cm}^{-1}$ , S#20) samples with the WFS  $8 \text{ m min}^{-1}$ . The difference in the average grain size between the unaffected BM and the HAZ 3 is shown in Fig. 11 b and d, from which it can be seen that the lower HI resulted in a smaller average grain size. Moreover, S#8 contains less ferrite (white needle-shaped area) and more lath martensite (dark needle-shaped area) than S#20 in the HAZ 1 (Fig. 11 a and c) and smaller grain size in the HAZ 3 (Fig. 11 b and d) due to the lower HI during the weld overlay.

Figure 12 shows that the total and maximum HAZ thickness (i.e., HAZ 1 + 2 + 3) increased with increasing welding heat input. Furthermore, as a result of increasing the WFS at a constant heat input, the HAZ thickness is decreased as more heat is required to melt the increased filler wire mass, revealing an inverse relationship between the WFS and the HI in this study.

#### 3.4 The weld metal

The microstructure obtained as the weld cools from the liquid phase to ambient temperature is called the as-deposited or primary microstructure. The as-deposited microstructure of the alloy IN686 claddings (or the weld metal) is comprised of a  $\gamma$ -FCC matrix with precipitation of secondary phases in the intercellular and interdendritic regions. The

**Fig. 10** Optical micrographs of a weld overlay sample in **a** WZ-HAZ 1, **b** HAZ 2, **c** HAZ 3, **d** transitional zone, **e** the unaffected base metal, and **f** SEM micrographs of the base metal



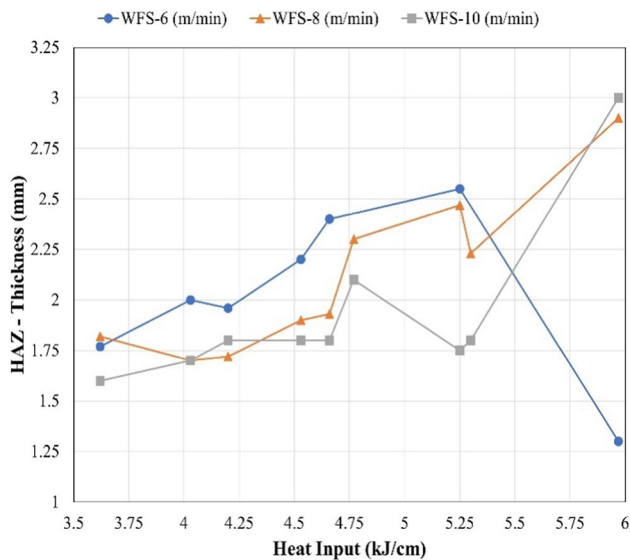
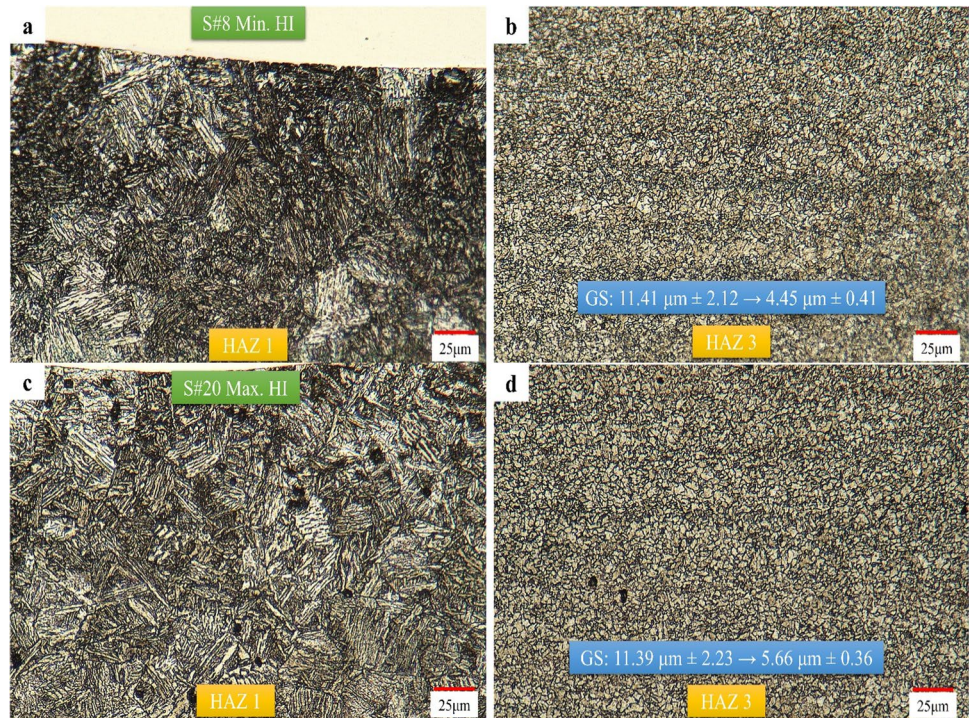
solidification microstructure was affected by the cooling rate changes (i.e., variations in the solid–liquid growth rate ( $R$ ) and thermal gradient ( $G$ ) which, consequently, affects the cooling rate ( $G \times R$ ) from the weld interface or the weld zone toward the top surface of the overlay.

Figure 13 shows the solidification morphologies of the weld metal for two samples with the minimum (HI:  $3.62 \text{ kJ cm}^{-1}$ , S#8) and the maximum (HI:  $5.97 \text{ kJ cm}^{-1}$ , S#20) heat input for the WFS  $8 \text{ m min}^{-1}$ . The microstructure of the cladding layer was analyzed in three areas: the top part (T), the middle part (M), and the bottom part (B) of the WZ. As can be seen from the figure, the bottom area includes planar, cellular, and columnar dendritic grain structures, which suggests a rapid change in  $G/R$  in this region. The middle area contains a dendritic structure elongated in the direction of the maximum thermal gradient (i.e., roughly perpendicular to the weld interface). The top area contains an equiaxed dendritic structure with secondary and tertiary arms.

Figure 13 reveals that the HI altered the solidification morphology, specifically dendrite arm spacing (DAS). The DAS for all samples was measured in the B area (for primary dendrite arms). The DAS variations against the heat input are presented in Fig. 14 and Table 5. As can be seen from the Fig. 14, the DAS increased with increasing heat input. Besides, the average DAS is almost decreased with increasing the WFS at the constant heat input although all the data begins to overlap if the reported standard deviation in Table 5 considered. However, the WFS can be seen to have a non-significant effect on the DAS when the heat input was constant. With increasing the WFS, at constant heat input, the bead width increased (Table 4), causing faster cooling due to more contact area with the BM at the weld interface and, therefore, a corresponding decrease in the DAS.

The SEM analysis of the weld metal (Fig. 15) reveals that the DAS affects the microsegregation of alloying elements and, consequently, the volume fraction of interdendritic and

**Fig. 11** Optical micrographs of **a, c** the HAZ 1 and **b, d** HAZ 3 in weld samples by the **a, b** minimum (S#8) and **c, d** the maximum heat input (S#20)



**Fig. 12** Variation of the total HAZ thickness with the welding heat input and WFS

intercellular precipitates. Figure 15 shows SEM micrographs of S#8 and S#20, which were welded by the minimum and the maximum heat input, respectively. It can be seen that a greater volume fraction and chain and elongated-shapes of intercellular particles are present within the sample with the higher HI (S#20).

Table 6 presents the volume fraction of interdendritic precipitates in the bottom areas of samples welded with WFS

of  $8 \text{ m min}^{-1}$ . Besides, the partition coefficient ( $k = \frac{C_s}{C_0}$ , which is derived from the Scheil equation) for the main elements were calculated for each sample, where  $C_s$  is the composition of solid at the beginning of solidification and  $C_0$  is the chemical composition of the liquid, and it is considered to be the nominal composition of the weld metal. The values of the  $k$  obtained for Ni, Fe, and W were greater than 1, which shows the tendency of these elements of being incorporated into the solid. The  $k$  values for Mo and Cr were less than 1 in all overlays, which indicates their tendency to segregate into the liquid metal and interdendritic zones during solidification. The decrease of  $k$  for Mo with the increase of dilution (i.e., with increasing heat input) has been observed previously; Mina et al. [10] reported that Mo increased its segregation potential as dilution increased. Cr and W followed a similar behavior, showing a slight decrease of the coefficient  $k$  as dilution increased. Maltin et al. [4] also observed that the coefficient  $k$  of W decreased with the increase of dilution of IN686. In a similar way, this reduction of the coefficient  $k$  of Cr with the increase of dilution has been also reported in previous investigations [10, 24].

Furthermore, the increase in heat input from sample #8 to #20 led to a twofold increase in the volume fraction of interdendritic precipitates from 0.82 to 1.65%, respectively (Fig. 15 and Table 6), and the precipitated particles were enriched with Mo and Cr. These precipitates are elongated in the direction of solidification in the bottom area. Silva et al. [8] reported that precipitation of secondary phases in

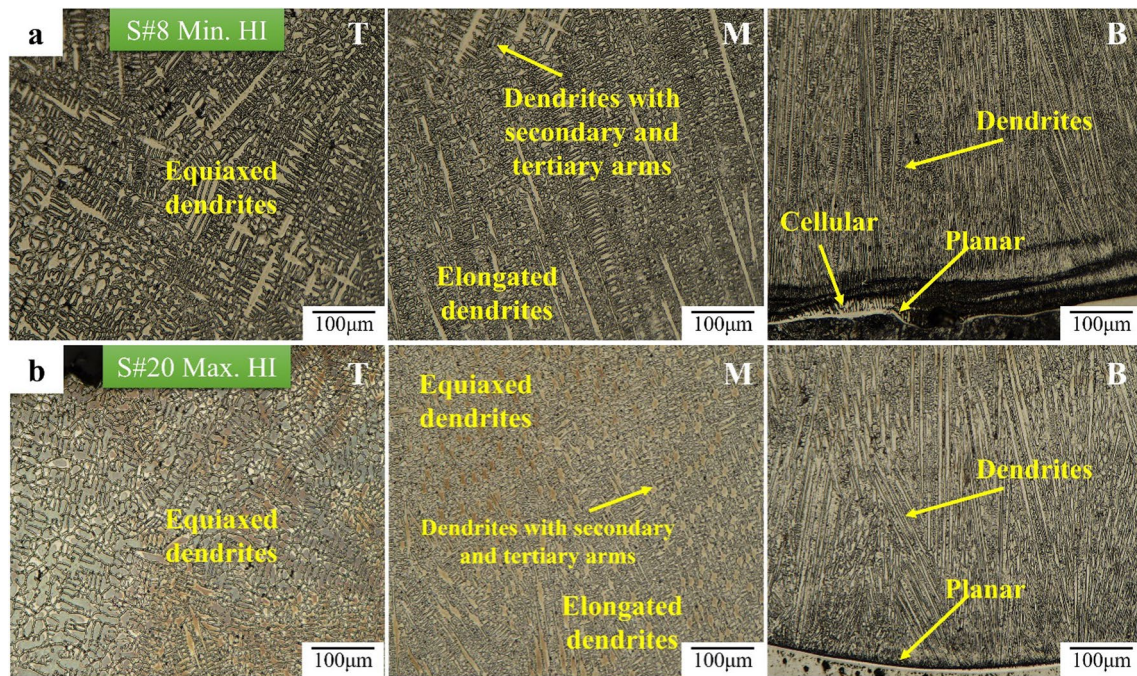


**Fig. 13** Microstructural evolution of the weld metal with inducing **a** minimum and **b** maximum welding heat input from the top surface (T) toward the bottom part (B) of the weld overlay

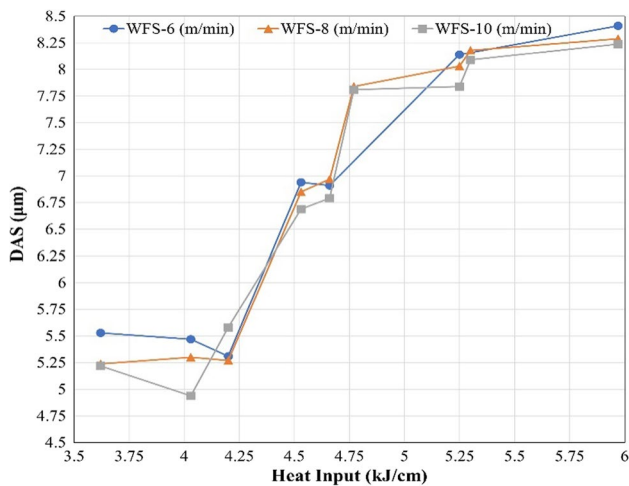


**Fig. 14** Variation of DAS with the HI and the WFS in the bottom part (B) of the IN686 weld metal

intercellular regions and interdendritic solidification grain boundaries are formed as a result of different levels of microsegregation of various elements during solidification, in particular Mo.

Figure 16 shows the segregation of Mo and Cr in intercellular/interdendritic zones. The chemical analysis of an exemplary precipitate with this elongated morphology in the intercellular/interdendritic area revealed a slight reduction in Ni content and an increase in the concentration of Mo,

indicating that it is a Mo-rich TCP phase. However, it should be noted that the chemical analysis by EDS was difficult due to the small size of the secondary phase plates. Nevertheless, the EDS analysis revealed that the chain-like and large precipitates contain Mo: 32–38 wt.%, Ni: 34–38 wt.%, Fe: 6–7 wt.%, Cr: 21–23 wt.%, and W: 4.0–4.5 wt.%, which is close to the chemical composition of the  $\sigma$  phase in welded IN686 as reported by [8]. The composition of fine particles contains Mo: 42–48 wt.%, Ni: 24–27 wt.%, Fe: 4–5 wt.%, Cr: 15–17 wt.%, and W: 6–7 wt.%, which is close to the reported chemical composition for the P-phase [8, 10]. Although the  $\mu$ -phase was not observed in this study, the cooling rates achieved during the welding process (i.e., indirect relation to the heat input [25]) are significantly high, and the material remains for a short period of time in the transformation temperature range, allowing only a partial phase transformation of the P-phase into the  $\mu$ -phase [8, 10, 25].

### 3.5 Microhardness

The average measured Vickers hardness values in different zones for weld overlay samples fabricated with a WFS of 8 m min<sup>-1</sup> can be seen in Fig. 17 as a function of the heat input. The hardness value of the unaffected base material was similar in all samples at  $168 \pm 2.3$  HV and is not shown in the Fig. 17. In general, the hardness values decreased with increasing welding heat input. For samples welded by heat inputs from 3.62 to 4.65 kJ cm<sup>-1</sup>, the

**Table 5** Variation of DAS and its standard deviation with the HI and the WFS in the bottom part (B) of the IN686 weld metal for each sample#

S# for WFS-6	HI (kJ/cm)	DAS ( $\mu\text{m}$ )	( $\pm$ )
7	3.62	5.53	0.72
4	4.03	5.47	0.57
16	4.20	5.31	0.44
1	4.53	6.94	0.52
13	4.66	6.91	0.52
10	5.25	8.14	0.92
19	5.97	8.41	0.88
S# for WFS-8			
8	3.62	5.24	0.37
5	4.03	5.3	0.89
17	4.20	5.27	0.53
2	4.53	6.85	0.61
14	4.66	6.97	0.43
26	4.77	7.84	0.42
11	5.25	8.03	0.89
23	5.30	8.18	0.77
20	5.97	8.29	0.56
S# for WFS-10			
9	3.62	5.22	0.48
6	4.03	4.94	0.68
18	4.20	5.58	0.62
3	4.53	6.69	0.59
15	4.66	6.79	0.65
27	4.77	7.81	0.34
12	5.25	7.84	0.48
24	5.30	8.09	0.91
21	5.97	8.24	0.34

hardness values in HAZ 1 were higher than the WZ (weld metal near to the weld interface) and the top surface of the weld metal due to the higher cooling rates (i.e., induced by the lower heat input), which caused the formation of lath martensite and upper bainite in the HAZ 1, despite of having larger grains than HAZ 2 or HAZ 3 (Figs. 10 and 11). The hardness values of welded samples with a heat input greater than  $4.65 \text{ kJ cm}^{-1}$  in HAZ1 were reduced from 295.5 HV to the range of (232–246.5 HV), which are close to the hardness range of the weld metal in near to the weld interface (233–239 HV).

The hardness values in the weld metal (near to the weld interface or WM + WZ) were measured to be  $\sim 5\%$  higher than at the top surface of the weld metal (Top WM) in all samples. This difference is attributed to the higher cooling rate adjacent to the base material (in weld interface) and the effect of thermal gradient between the previous melt tracks and the track surfaces during welding and solidification. The hardness continuously decreased in the HAZ 2

( $\sim 243$  to  $\sim 218$  HV) and the HAZ 3 ( $\sim 213$  to 189 HV) by increasing the weld heat input.

## 4 Discussion

### 4.1 Weld quality

Good quality welds should be defect-free and without any surface cracks. No cracks were observed during the visual inspection of all welded samples in the current study. However, Fig. 4 and Table 3 indicate that some of the welded plates exhibited surface porosity, discrete weld lines, and spattering. The micrographs in Fig. 18 a and b reveal that spatter caused cracks in the overlapping boundary and porosity formation in the weld interface due to changing the cooling rate in the substrate, and they hindered the formation of a complete joint between the molten weld pool and the base material. The same defects were observed in samples welded using a HI of  $4.5\text{--}6 \text{ kJ cm}^{-1}$  and WFS of  $10 \text{ m min}^{-1}$ .

The results presented in Fig. 6 showed that the WFS parameter significantly affected (i.e., increased) the bead height or reinforcement. On the other hand, there was no significant decrease in the penetration of the bead with the increase of the WFS. This was due to the fact that as the WFS increases (at a fairly constant welding current) the size of molten drops of filler wire deposited on the base metal increases which reduces the heat input (i.e., increasing thermal gradient) and increases the cooling rate to the base metal. Therefore, the penetration decreases or was nearly constant, since penetration is largely determined by arc pressure, which is a function of current density [26, 27]. An increase in penetration due to an increase in HI is attributed to the fact that the molten filler wire easily penetrates the base metal and fusion takes place. As a result, an increase in the WFS, at a constant HI, results in more reinforcement for the overlaid plates.

Table 4 revealed that the bead width is dominated by the HI and the WFS. The higher voltages cause the bead to widen, since higher voltages induce high heat inputs, therefore, reducing the viscosity of the weld pool and increasing the tendency of the molten filler wire to flow and produce a wider weld bead as has been reported by [28]. Although the bead width can be reduced by increasing the TS with constant voltage, a simultaneous increase in the voltage (19, 22, 25 V) and the TS ( $40.6, 45.7, 50.8 \text{ cm min}^{-1}$ ) resulted in the bead width increasing, which indicates the dominant role of voltage in controlling the bead width (see samples #2, #14, and #26, voltage and TS are increased with constant WFS of  $8 \text{ m min}^{-1}$ ).

Besides, Table 4 and Fig. 7 revealed that the level of dilution induced by the GMAW parameters is another parameter that must be considered to optimize the GMAW overlay

**Fig. 15** SEM micrographs of the bottom (B) and the top (T) areas of the weld metal in **a** S#8 ( $HI=3.62 \text{ kJ cm}^{-1}$ ) and **b** S#20 ( $HI=5.97 \text{ kJ cm}^{-1}$ ) welded by the maximum heat input

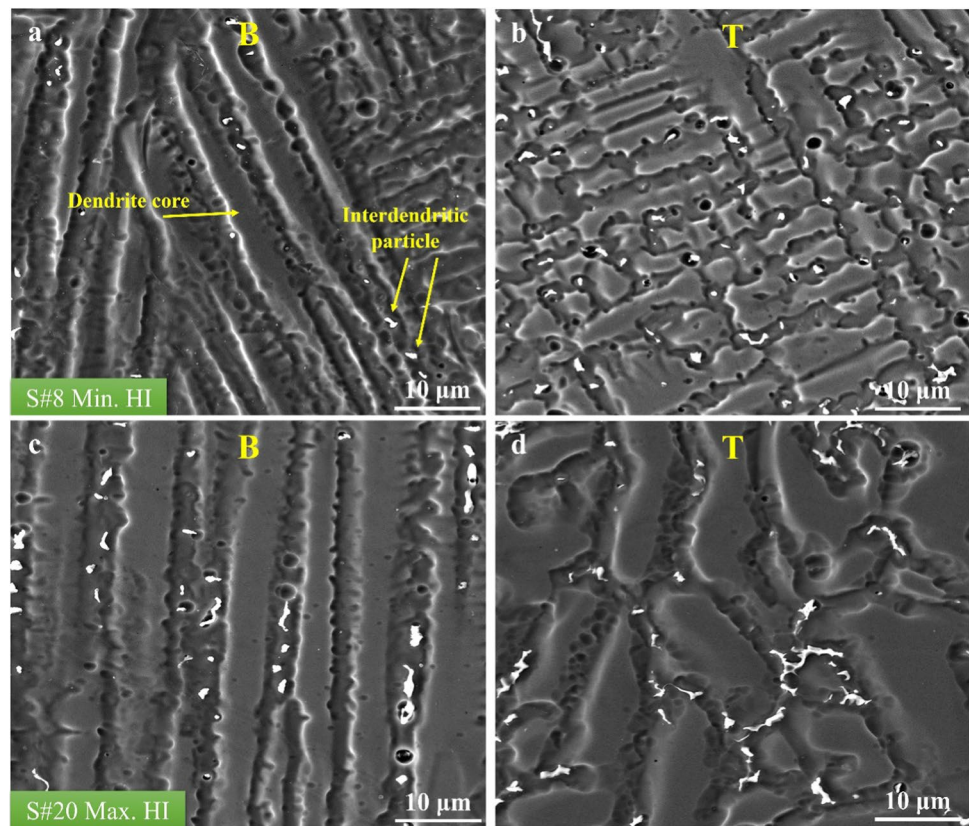


**Table 6** Partition coefficient ( $k$ ) of the main alloying elements and volume fraction of interdendritic phases present in the weld metal of the weld overlay samples with the WFS of  $8 \text{ m min}^{-1}$

S#	Partition Coefficient ( $k$ )					Volume Fraction (%)
	Cr	Fe	Mo	Ni	W	
8	0.974	1.041	0.892	1.060	1.071	$0.82 \pm 0.13$
5	0.963	1.091	0.884	1.032	1.068	$0.96 \pm 0.11$
17	0.966	1.014	0.885	1.019	1.031	$1.29 \pm 0.21$
2	0.967	0.901	0.877	1.105	1.027	$1.32 \pm 0.18$
14	0.951	1.063	0.869	1.075	1.022	$1.39 \pm 0.17$
26	0.952	0.932	0.841	1.102	1.045	$1.37 \pm 0.14$
11	0.956	1.106	0.827	1.069	1.019	$1.44 \pm 0.09$
23	0.948	1.031	0.813	1.054	1.021	$1.46 \pm 0.22$
20	0.928	1.046	0.777	1.070	1.015	$1.65 \pm 0.21$

parameters. Welding parameters such as HI and WFS had effects on the weld quality and the microstructure, and these parameters could change the segregation potential and dilution (e.g., Table 4). Arulmurugan and Manikandan [29] observed similar results by optimizing GTAW parameters in the weld overlay of IN686 alloy. Increasing dilution levels and, consequently, Fe concentrations in weld metal aggravated the microsegregation of Mo and Cr, resulting in a decrease in their  $k$  values [8, 30]. More dilution and microsegregation of Mo and Cr can reduce the welding quality and corrosion resistance of the overlay [8, 11, 16, 31, 32]. Hence, the present study confirms that the process parameters

employed to fabricate overlay IN686 alloy on low-carbon steel plates can be optimized by selecting parameters that reduce heat input, dilution, and, therefore, microsegregation.

Therefore, regarding the results of the visual examination, weld geometries, and microscopic evolution of the 27 welded samples produced with various conditions, the weld overlay of IN686 superalloy by automatic GMAW process is optimized and the process map is plotted in Fig. 19 according to the successfully welded samples, the dilution level, and the weld heat input, and those with different micro- and macroscopic defects. The weld overlays of IN686 produced using WFS of 6 and  $8 \text{ m min}^{-1}$  and the mid-level

**Fig. 16** EDS line scan analysis in the dendritic and interdendritic area of the bottom area of welded sample #20 with Mo-rich TCP phase

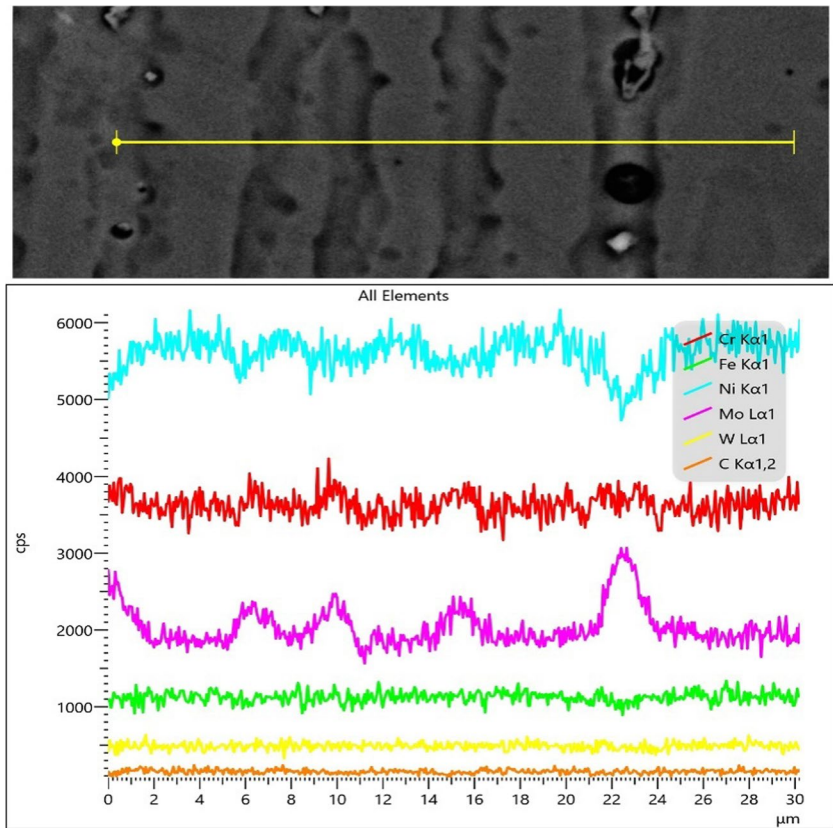
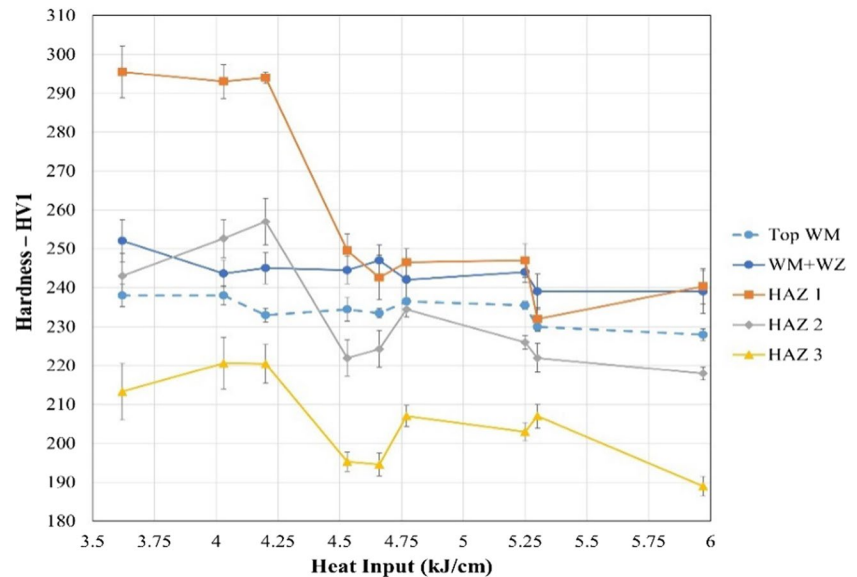


**Fig. 17** Vickers hardness (HV1) variation in different welding zones with the heat input in samples welded using a WFS of  $8 \text{ m min}^{-1}$



HI ( $4\text{--}5 \text{ kJ cm}^{-1}$ ) resulted in the best cladding quality. The lower HI conditions resulted in porosities and cracks in the weld interface and eventually lack of fusion between the weld metal and the base material. Overlays with HIs higher than  $4 \text{ kJ cm}^{-1}$  and by the greatest WFS ( $10 \text{ m min}^{-1}$ ) produced weldments with more porosities and spatters on the surface, which decreased the surface quality; however, the

dilution was significantly lower than weldments produced by the WFS  $6 \text{ m min}^{-1}$ . Weld overlays with the high level of the HIs ( $4.5\text{--}6 \text{ kJ cm}^{-1}$ ), in this study, resulted in three different behaviors: (1) no weld or no joint was obtained from samples with the lowest feeding rate ( $6 \text{ m min}^{-1}$ ); (2) welded samples by the WFS  $8 \text{ m min}^{-1}$  induced high levels of dilution which is undesirable regarding the mechanical



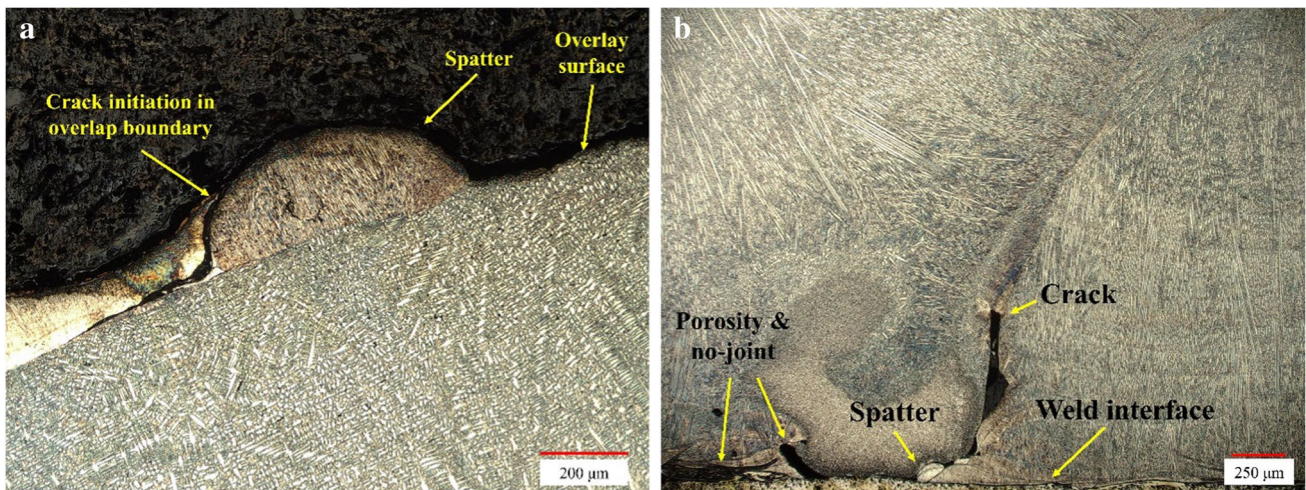
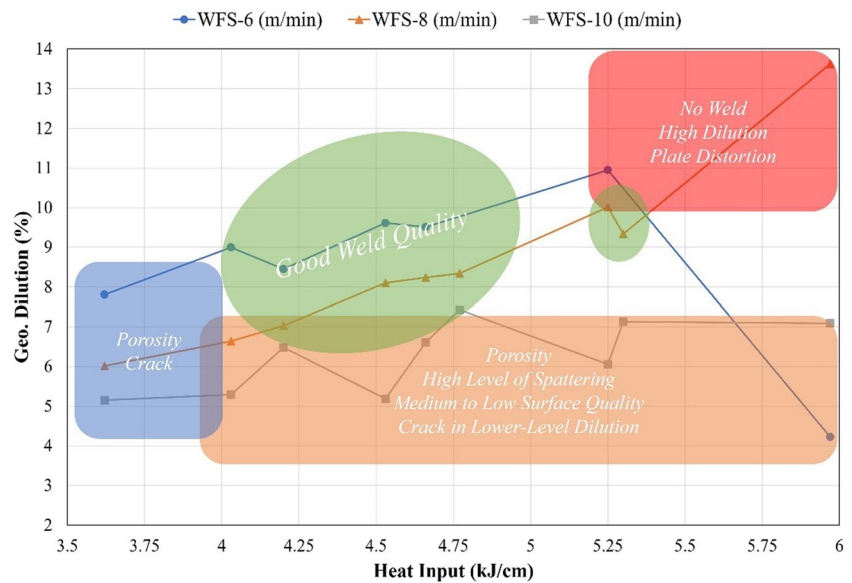


**Fig. 18** Optical images of spatters formed during welding of S#3 and its effects on **a** welding surface and overlap boundary, and **b** porosity formation and lack of fusion at the weld interface

**Fig. 19** Process map of auto-matic GMAW weld overlay of IN686 superalloy on low-carbon steel SA516-Gr.70



properties of the cladding layer, and its corrosion resistance; and (3) although welded samples produced by the WFS 10 m min<sup>-1</sup> reduced the dilution level, it led to more spattering during welding (Tables 3 and 4, Fig. 18), which detrimentally affected the overlap layer by inducing cracks in the overlap boundaries and inhibiting the complete joints between the weld metal and the base material.

### 4.2 Microstructure examination

The microstructure of the weld metal (Fig. 13) was comprised of elongated grains (dendritic structure) and equiaxed grains (or dendrites) in the bottom area and the top area of the weld metal, respectively, due to the variation of *G* and *R* throughout the weld pool. Moreover, as shown in Fig. 14,

the DAS increased with increasing weld heat input because of slower cooling rates during solidification. Mina et al. [10] calculated the cooling rate as a result of the GTAW process (with dilution of more than 20%) by using Rosenthal’s equation (Eq. 4) for three dimensions to predict the cooling rate in the overlay:

$$\frac{\partial T}{\partial t} = \frac{2\pi \cdot \lambda \cdot TS(T - T_0)^2}{\eta \cdot V \cdot I} \tag{4}$$

where the cooling rate ( $\frac{\partial T}{\partial t}$ ) is based on thermal conductivity ( $\lambda$ ), welding travel speed (*TS*), beginning of solidification temperature (*T*) and pre-heating and/or inter-pass temperature (*T*<sub>0</sub>), electric arc efficiency ( $\eta$ ) (~0.85 for GMAW), and of the arc voltage (*V*) and current (*I*). However, this equation

cannot embrace the effect of various WFS on the cooling rate in this study. The effect of the WFS on the DAS is plotted in Fig. 14, where it can be seen that WFS generally has a negligible effect on DAS. Therefore, the primary DAS, near to the weld interface, was measured through SEM and optical microscopy analysis and was applied in the empirical Eq. 5 to obtain the cooling rate ( $\dot{\epsilon}$  or  $\frac{\partial T}{\partial t}$ ) [25, 33]:

$$DAS_{(\mu\text{m})} = 518.39(\dot{\epsilon})^{-0.592} \quad (5)$$

In which the model constant values were assumed to be the same as IN718 because IN686 has almost similar thermal behavior as IN718 superalloy [25, 33, 34]. As a result, the cooling rate for the lowest weld heat input (S#8, HI = 3.62 kJ cm<sup>-1</sup>) was calculated to be  $2.35 \times 10^3$  °C s<sup>-1</sup> while the calculated value for the highest heat input sample (S#20, HI = 5.97 kJ cm<sup>-1</sup>) was  $1.08 \times 10^3$  °C s<sup>-1</sup>. The slower cooling rate in S#20 provides more time for Fe dilution and Cr and Mo segregation. As shown in Figs. 7 and 15 and presented in Tables 4 and 6, reducing the cooling rate or increasing the heat input increases the dilution (both Geo. D and Com. D), Cr and Mo segregation, and the interdendritic secondary phases.

The effects of dilution on the partition coefficient (*k*) are partially associated with the phenomenon of the solubility reduction of Cr, Mo, and ~W in the new matrix  $\gamma$ -FCC that now contains more iron. The phase diagrams for binary Ni-Mo, Fe-Mo, Ni-Cr, Fe-Cr, Ni-W, and Fe-W alloys show some differences in the solubility of the elements Mo, Cr, and W into the  $\gamma$ -Ni and  $\gamma$ -Fe matrices [10, 35]. Besides, the hardness results (Fig. 17) illustrate that in the samples with the higher heat input (and more dilution), the hardness of the HAZ 1 is reduced because of depletion Fe (Fe dilution in the weld metal) and less martensite formation (Fig. 11 a and c) in this zone during rapid solidification and phase transformation. The dilution of Fe into the weld metal also reduced the hardness due to the formation of detrimental and brittle TCP phases which can substantially decrease the solid solution strengthening of the alloy [8, 36, 37].

The presence of elongated chains of precipitates in the intercellular regions (Fig. 15 c) can significantly impair the mechanical properties of the weld overlay not only because they are brittle phases, but also due to their orientation, providing a preferential path for crack propagation which has been also reported by [5, 8, 10, 16, 29]. As for the columnar dendritic growth in the middle of the weld metal, the volumes for the formation of secondary phases became narrower due to the growth of secondary arms, which help to break the continuity of the secondary phases, making smaller particles and a more tortuous crack propagation path.

## 5 Conclusions

The present study aims to understand how welding process parameters affect the quality and microstructure of the weld overlay and optimize weld overlay parameters. Based on the results obtained and presented in this study on the visual examination and the microstructural characteristics of dissimilar weld overlays with Inconel 686 superalloy deposited by the automatic GMAW process with automatic cold wire feeding on low-carbon steel plates, it was concluded that:

- The IN686 overlay on low-carbon steel by the low and mid-levels of wire feeding speeds and the mid-level of HI (4–5 kJ cm<sup>-1</sup>) resulted in defect-free clad plates with the optimum surface quality (as compared to other conditions) and the low amount of interdendritic/intercellular secondary phases.
- The bead width is dominated by the voltage more than the travel speed and the wire feed speed affects the reinforcement more than the penetration.
- Low levels of welding dilution reduce the microsegregation tendency of Cr and Mo in interdendritic areas which can improve clad layer mechanical and corrosion performance.
- Increasing the heat input increased the DAS by reducing the cooling rate (increasing solidification time) which causes more elemental segregation in interdendritic areas and samples containing higher amounts of secondary or TCP phases.
- The hardness of base metal areas is substantially affected and reduced by increasing the heat input, due to increasing the dilution of Fe from the base material to the weld metal (Fe depletion in HAZ 1), and the heat-affected zone thickness increases with increasing heat input.

**Acknowledgements** The authors gratefully acknowledge the financial support of the MITACS Accelerate program (Mitacs Accelerate IT29864) and Teck Resources Trail operations. They would like to express their gratitude to George Gemell from CIMS Ltd., for welding the plates and for discussing designing welding conditions. They would also like to acknowledge Dr. Sudip Shrestha of the Fipke Lab for Trace Element Research (FiLTER) at UBC Okanagan for his assistance with the SEM analysis.

**Author contribution** Seyedmohammad Tabaie: investigation, analysis, and writing. Trevor Greene: advice and revising. Michael J. Benoit: advice, revising, and supervision.

**Funding** This work was supported by MITACS Accelerate program (Grant numbers Mitacs Accelerate IT29864). Authors S. Tabaie and M. J. Benoit have received research support from MITACS and Teck Resources Ltd.

## Declarations

**Competing interests** The authors declare no competing interests.

## References

- Tayactac RG, Ang EBO (2021) A review of corrosion resistance alloy weld overlay cladding material for geothermal applications. *Mater Sci Forum* 1047:120–127. <https://doi.org/10.4028/www.scientific.net/MSF.1047.120>
- Wang SH, Jiang J, Tadic D, McKinnell's J (2016) Weld cladding for mining and mineral processing: a Canadian perspective. *CWA J* 8:52–66
- A. Volpi, G. Serra (2018) Weld overlay of highly corrosion resistant nickel chromium molybdenum alloys, UNS N06059, on low alloy equipment operating at high temperature. ASME 2018 Symposium on Elevated Temperature Application of Materials for Fossil, Nuclear, and Petrochemical Industries Seattle, WA, USA. <https://doi.org/10.1115/etam2018-6715>
- Maltin CA, Galloway AM, Mweemba M (2014) Microstructural evolution of Inconel 625 and Inconel 686CPT weld metal for clad carbon steel linepipe joints: a comparator study. *Metall Mater Trans A* 45:3519–3532. <https://doi.org/10.1007/s11661-014-2308-z>
- Arulmurugan B, Sathishkumar M, Gokulkumar K, Mageshkumar K, Subramani P, Venkateshkannan M, Manikandan A (2018) Welding metallurgy of corrosion resistant 21st century Ni-based superalloy 686. Springer International Publishing, Cham, pp 457–463
- Mehta MV, Vora JJ, Chaudhari MD (2021) A review of challenges to hastelloy – C series weld overlay. In: *Recent advances in mechanical infrastructure*, pp 157–172. [https://doi.org/10.1007/978-981-33-4176-0\\_13](https://doi.org/10.1007/978-981-33-4176-0_13)
- Winowlin Jappes JT, Ajithram A, Adamkhan M, Reena D (2022) Welding on Ni based super alloys—a review. *Mater Today Proc* 60:1656–1659. <https://doi.org/10.1016/j.matpr.2021.12.208>
- Silva CC, Afonso CRM, Ramirez AJ, Motta MF, Miranda HC, Farias JP (2016) Assessment of microstructure of alloy Inconel 686 dissimilar weld claddings. *J Alloys Compd* 684:628–642. <https://doi.org/10.1016/j.jallcom.2016.05.231>
- Adamiec P, Adamiec J (2007) Aspects of pad welding of waste-incinerator boiler-elements with Inconel 625 and 686 alloys. *Weld Int* 21:190–194. <https://doi.org/10.1533/wint.2007.3753>
- Miná EM, da Silva YC, Dille J, Silva CC (2016) The effect of dilution on microsegregation in AWS ER NiCrMo-14 alloy welding claddings. *Metall Mater Trans A* 47:6138–6147. <https://doi.org/10.1007/s11661-016-3786-y>
- Hayes JR, Gray JJ, Szmodis AW, Orme CA (2006) Influence of chromium and molybdenum on the corrosion of nickel-based alloys. *Corrosion* 62:491–500. <https://doi.org/10.5006/1.3279907>
- Frei J, Alexandrov BT, Rethmeier M (2018) Low heat input gas metal arc welding for dissimilar metal weld overlays part II: the transition zone. *Weld World* 62:317–324. <https://doi.org/10.1007/s40194-017-0539-5>
- Singh Singhal T, Kumar Jain J (2020) GMAW cladding on metals to impart anti-corrosiveness: Machine, processes and materials. *Mater Today Proc* 26:2432–2441. <https://doi.org/10.1016/j.matpr.2020.02.518>
- Rajkumar V, Arjunan TV, Rajesh Kannan A (2019) Metallurgical and mechanical investigations of Inconel 625 overlay welds produced by GMAW-hardfacing process on AISI 347 pipes. *Mater Res Express* 6. <https://doi.org/10.1088/2053-1591/ab11f0>
- A. N., O. R., K. P. (2015) Effect of GMAW process parameters on the influence of bead geometry and HAZ area on ASTM A516 grade 70 Low alloy Pressure vessel steel. *Int. J. TechnoChem Res.* 01: 01-10
- Najafi M, Moshkbar Bakhshayesh M, Farzadi A (2021) Microstructure and phase analysis of multilayer Ni–Cr–Mo clad for corrosion protection. *Trans Indian Inst Met* 74:1663–1672. <https://doi.org/10.1007/s12666-021-02256-z>
- Petrzak P, Kowalski K, Rozmus-Górnikowska M (2017) Microstructure and chemical composition of Inconel 625 and 686 weld overlays deposited by CMT on 16Mo3 steel. *Przegląd Spawalnictwa* 89:24–29
- Karimi MR, Wang SH, Jelovica J (2022) Taguchi-based experimental investigation into weld cladding of Ni-WC MMC overlays by CMT process. *Int J Adv Manuf Technol* 122:2433–2461. <https://doi.org/10.1007/s00170-022-09816-7>
- ASTM E1245-03 (2016) Standard practice for determining the inclusion or second-phase constituent content of metals by automatic image analysis. American Society for Testing and Materials, pp 1–8. <https://doi.org/10.1520/E1245-03R16>
- Sun YL, Hamelin CJ, Vasileiou AN, Xiong Q, Flint TF, Obasi G, Francis JA, Smith MC (2020) Effects of dilution on the hardness and residual stresses in multipass steel weldments. *Int J Press Vessels Pip* 187. <https://doi.org/10.1016/j.ijpvp.2020.104154>
- Taraphdar PK, Mahapatra MM, Pradhan AK, Singh PK, Sharma K, Kumar S (2021) Evaluation of through-thickness residual stresses and microstructure in SA516 Gr. 70 steel welds. *Proc Inst Mech Eng Part B: J Eng Manuf* 235:958–973. <https://doi.org/10.1177/0954405421990124>
- Prajapati PJ, Badheka VJ (2019) Investigation on three different weldments on performance of SA516 Gr70 steel material. *Alexandria Eng J* 58:637–646. <https://doi.org/10.1016/j.aej.2019.05.012>
- Huang K, Logé RE (2016) A review of dynamic recrystallization phenomena in metallic materials. *Mater Des* 111:548–574. <https://doi.org/10.1016/j.matdes.2016.09.012>
- Banovic SW, Dupont JN, Marder AR (2013) Dilution and microsegregation in dissimilar metal welds between super austenitic stainless steel and nickel base alloys. *Sci Technol Weld Joining* 7:374–383. <https://doi.org/10.1179/136217102225006804>
- Zhang Y, Huang B, Li J (2013) Microstructural evolution with a wide range of solidification cooling rates in a Ni-based superalloy. *Metall Mater Trans A* 44:1641–1644. <https://doi.org/10.1007/s11661-013-1645-7>
- A. N., O. R., K. P. (2015) Effect of GMAW process parameters on the influence of bead geometry and HAZ area on ASTM A516 grade 70 Low alloy Pressure vessel steel. *Int. J. TechnoChem Res.* 01: 01-10
- Abdollah-zadeh A, Nouri M, Malek F (2007) Effect of welding parameters on dilution and weld bead geometry in cladding. *J Mater Sci Technol* 23:817–822
- Murugan N, Parmar RS (1994) Effects of MIG process parameters on the geometry of the bead in the automatic surfacing of stainless steel. *J Mater Process Technol* 41:381–398
- Arulmurugan B, Manikandan M (2018) Improvement of metallurgical and mechanical properties of gas tungsten arc weldments of alloy 686 by current pulsing. *Trans Indian Inst Met* 71:2953–2970. <https://doi.org/10.1007/s12666-018-1395-8>
- Manikandan M, Arivazhagan N, Nageswara Rao M, Reddy GM (2014) Microstructure and mechanical properties of alloy C-276 weldments fabricated by continuous and pulsed current gas tungsten arc welding techniques. *J Manuf Processes* 16:563–572. <https://doi.org/10.1016/j.jmapro.2014.08.002>

31. Solecka M, Kusiński J, Kopia A, Rozmus-Górnikowska M, Radziszewska A (2016) High-temperature corrosion of Ni-base alloys by waste incineration ashes. *Acta Phy Pol A* 130:1045–1048. <https://doi.org/10.12693/APhysPolA.130.1045>
32. Adamiec J (2009) High temperature corrosion of power boiler components clad with nickel alloys. *Mater Charact* 60:1093–1099. <https://doi.org/10.1016/j.matchar.2009.03.017>
33. Manikandan SGK, Sivakumar D, Rao KP, Kamaraj M (2014) Effect of weld cooling rate on Laves phase formation in Inconel 718 fusion zone. *J Mater Process Technol* 214:358–364. <https://doi.org/10.1016/j.jmatprotec.2013.09.006>
34. Patel AD, Erbrick J, Heck K, Maurer G (2012) Microstructure development during controlled directional solidification in alloy 718. In: *Superalloys 2012*. TMS, pp 595–600. <https://doi.org/10.1002/9781118516430.ch66>
35. Baker H (1992) *Alloy phase diagrams*. ASM International, Ohio
36. Turchi PEA, Kaufman L, Liu Z-K (2007) Modeling of Ni–Cr–Mo based alloys: Part II — Kinetics. *Calphad* 31:237–248. <https://doi.org/10.1016/j.calphad.2006.12.006>
37. Turchi PEA, Kaufman L, Liu Z-K (2006) Modeling of Ni–Cr–Mo based alloys: Part I—phase stability. *Calphad* 30:70–87. <https://doi.org/10.1016/j.calphad.2005.10.003>

**Publisher's note** Springer Nature remains neutral with regard to jurisdictional claims in published maps and institutional affiliations.

Springer Nature or its licensor (e.g. a society or other partner) holds exclusive rights to this article under a publishing agreement with the author(s) or other rightsholder(s); author self-archiving of the accepted manuscript version of this article is solely governed by the terms of such publishing agreement and applicable law.